quantum beam science

MDPI

Article

Simulation Dosimetry Studies for FLASH Radiation Therapy (RT) with Ultra-High Dose Rate (UHDR) Electron Beam

Nick Gazis [1,2,*], Andrea Bignami [1,2], Emmanouil Trachanas [1,2], Melina Moniaki [3], Evangelos Gazis [1,3], Dimitrios Bandekas [4] and Nikolaos Vordos [4]

[1] Institute of Accelerating Systems & Applications (IASA), 10024 Athens, Greece; andrea.bignami@ess.eu (A.B.); emmanuil.trachanas@ess.eu (E.T.); evangelos.gazis@cern.ch (E.G.)
[2] European Spallation Source (ESS) ERIC, P.O. Box 176, SE-221 00 Lund, Sweden
[3] Physics Department, Zografou Campus, National Technical University of Athens (NTUA), 15780 Athens, Greece; melinamoniaki@gmail.com
[4] Physics Department, Democritus University of Thrace (DUTH), St. Lucas, 65404 Kavala, Greece; dbandek@physics.duth.gr (D.B.); nvordos@physics.duth.gr (N.V.)
* Correspondence: nick.gazis@ess.eu

Abstract: FLASH-radiotherapy (RT) presents great potential as an alternative to conventional radiotherapy methods in cancer treatment. In this paper, we focus on simulation studies for a linear particle accelerator injector design using the ASTRA code, which permits beam generation and particle tracking through electromagnetic fields. Space charge-dominated beams were selected with the aim of providing an optimized generated beam profile and accelerator lattice with minimized emittance. The main results of the electron beam and ultra-high dose rate (UHDR) simulation dosimetry studies are reported for the FLASH mode radiobiological treatment. Results for the percentage depth dose (PDD) at electron beam energies of 5, 7, 15, 25, 50, 100 MeV and 1.2 GeV for Poly-methyl-methacrylate (PMMA) and water phantom vs. the penetration depth are presented. Additionally, the PDD transverse profile was simulated for the above energies, delivering the beam to the phantom. The simulation dosimetry results provide an UHDR electron beam under the conditions of the FLASH-RT. The performance of the beam inside the phantom and the dose depth depends on the linear accelerator beam's energy and stability.

Keywords: FLASH-RT; dosimetry; UHDR; PDD; ASTRA/FLUKA simulations

check for updates

Citation: Gazis, N.; Bignami, A.; Trachanas, E.; Moniaki, M.; Gazis, E.; Bandekas, D.; Vordos, N. Simulation Dosimetry Studies for FLASH Radiation Therapy (RT) with Ultra-High Dose Rate (UHDR) Electron Beam. *Quantum Beam Sci.* **2024**, *8*, 13. https://doi.org/10.3390/qubs8020013

Academic Editor: Andrew Stevenson

Received: 24 March 2024
Revised: 30 April 2024
Accepted: 16 May 2024
Published: 24 May 2024

1. Introduction

The continuous increase in cancer incidents in recent years has highlighted the need for advanced treatment methods. Radiation therapy has been an efficient method for treating tumors for the last 100 years [1]. A major part of the cancer patients receive radiation therapy during their treatment, employing charged particle beams with sufficient doses to arrest cancer growth and minimize the damage to surrounding healthy tissues. The charged particle irradiation can be divided into proton/carbon ion therapy [2], very-high-energy electrons—VHEE [3] and FLASH radiation therapy (FLASH-RT) [4]. The FLASH-RT represents an innovative approach to radiotherapy, exploiting the radiobiological phenomenon known as the FLASH effect [5,6] and offering the possibility to deliver an extremely high dose rate (>40 Gy/s) while minimizing adverse effects on normal tissues and organs that may be damaged. This characteristic leads to the damage of cancer cells while causing minimal damage to healthy tissue. The potential advantages of FLASH-RT in cancer treatment were first observed back in 1966 on mouse experiments, and interest in this method and its applications was re-spawned in 2014 in a study by Favaudon, V. et al. [7].

In this work, FLASH-RT has been studied using an electron applicator [8] at the beam dose delivery with the FLUKA simulation package [9]. The calculation of the dose–depth percentage in the phantom and the beam characteristics have been obtained for different

electron energies of 5, 7, 15, 25, 50, 100 MeV and 1.2 GeV for Poly-methyl-methacrylate (PMMA) and water phantom vs. the penetration depth.

2. Materials and Methods

2.1. FLASH-RT Conditions

The FLASH-RT provides a very fast pulse electron beam for cancer treatment, which reduces damage to normal tissues while being efficient in tumor cell destruction. Although the underlying mechanisms of the FLASH effect are not fully understood, initial research work with some experiments has shown that a very high dose rate in ultra-short radiation pulses does not affect normal cells, contrary to conventional (CONV) treatments. After some decades, the FLASH effect was investigated and reported by V. Favaudon [10], where the total dose was delivered to the patient in a very short time.

The FLASH-RT effect may be achieved under various beam characteristic conditions vs. conventional electron beam irradiation, as summarized in Table 1.

Table 1. FLASH-RT vs. conventional radiation therapy beams' characteristic conditions.

Beam Characteristics	Conventional RT	FLASH RT
Dose Per Pulse	~0.4 mGy	~1 Gy
Dose Rate	~10^2 Gy/s	~10^5 Gy/s
Mean Dose Rate	~0.1 Gy/s	~100 Gy/s
Total Treatment Time	~days/minutes	<500 ms

Typically, the FLASH-RT effect should provide a dose > 1 Gy, which is many orders of magnitude greater than the usual conventional electron pulse (<1 mGy/pulse) [11,12].

The FLASH-RT regime demands the irradiation conditions of the beam to necessarily have the following operational parameters [13,14]:

- Irradiation time $t_i < 100$ ms;
- Average dose rate $\overline{\dot{D}} > 100$ Gy/s;
- In-peak dose rate $\dot{D}p > 10^6$ Gy/s;
- Pulse repetition frequency PRF > 100 Hz;
- Dose per pulse > 1 Gy.

2.2. FLASH-RT Injector Design

The requirements on dose and irradiation time to enable the FLASH effect (see Table 1) pose stringent design constraints and technical challenges to the accelerator lattice parameters, photocathode and laser system design. In particular, the high current beam and accelerating gradient needed to achieve levels of several MeVs with a compact configuration challenge beam production and stability. Moreover, the required irradiation time from multiple angles is prohibitory for gantry rotation, and alternative schemes such as energy switching and spectrometer magnets must be considered. In the first stages of this study, we aim to focus on photocathode selection and laser parameters as well as achieving a sufficient degree of beam emittance growth control throughout the injector. The simulations for this study were performed using ASTRA (Space Charge Tracking Algorithm) [15], an open-source software package developed by DESY that permits beam generation and particle tracking through electromagnetic fields. ASTRA was particularly chosen for its ability to simulate space charge-dominated beams applicable for this study, with the aim of providing an optimized generated beam profile and accelerator lattice with minimized emittance. The photocathode material plays a pivotal role in an RF photoinjector as it defines the quantum efficiency (QE) of the electron source and consequently the intrinsic emittance. Semiconductor materials like Cesium Telluride (Cs_2Te) provide a quantum efficiency (QE) that is much larger in magnitude than metal photocathodes like copper (Cu) or magnesium (Mg), while the operational time of the metal photocathodes is huge relative to semiconductors [16]. RF photoinjectors have been developed for high-charge

electron beams (1–6 nC), such as the PHIN photoinjector [17–19] for the secondary beam of the CLIC facility and the PITZ [20] photoinjector at DESY for European XFEL. The Cs_2Te semiconductor photocathodes are employed with UV laser illumination due to their better performance in such conditions. The laser spot radius needs to be carefully tailored to avoid photocathode saturation. Using the saturation charge density that depends on the cathode surface field, a minimum radius of 0.9 mm for 1 nC and a 100 MV/m electron gun were used for the ASTRA simulations. The obtained laser and photocathode specifications are summarized in Table 2.

Table 2. The ASTRA simulation results for laser and photocathode parameters to achieve the FLASH-RT electron beam conditions.

Parameter	Unit	Value
Photocathode material	-	Cs_2Te
RMS laser spot size (XY)	mm	0.9
Laser pulse duration	ps	10
Laser rise/fall time	ps	7
Laser wavelength	nm	262 (UVC)
Laser photon energy	eV	4.73
Initial kinetic energy	eV	1.609
Beam charge	nC	1
Electric field at cathode	MV/m	99
Energy distribution		Isotropic
Longitudinal distribution		Uniform ellipsoid
Transverse distribution		Radial

The ASTRA simulation results are shown in Figures 1–4, with important parameter selections for the optimum injector operation. In Figure 1, the homogenous solenoid field Bz (T) shown as a black line and the magnetic field gradient dBr/dr (T/m) shown as a red line are presented vs. the beam axis for the first 5 m injector length. A short-length e-gun solenoid just after the photocathode and an injector solenoid with four parts in sequence were selected. The magnetic field was adequately focused on the electron beam after the photocathode along the injector.

The produced longitudinal electric field Ez (MV/m) is presented in Figure 2; it provides impressive homogeneity for a proportional electron beam acceleration.

Additionally, the transverse emittance is presented in Figure 3, where the electron beam is stabilized after the first 50 cm from its production and continues to the beamline.

In Figure 4, the average beam energy is shown for the first 5 m in the injector from the photocathode, with its characteristic proportionality after 1 m from the photocathode arriving at a final beam energy that exceeds 70 MeV.

The final simulation results with the specific characteristics of the e-gun and the injector elements, presented in Figures 1–4, have defined the FLASH-RT electron beam specifications, presented in Table 2, which were necessary for the electron dosimetry simulations.

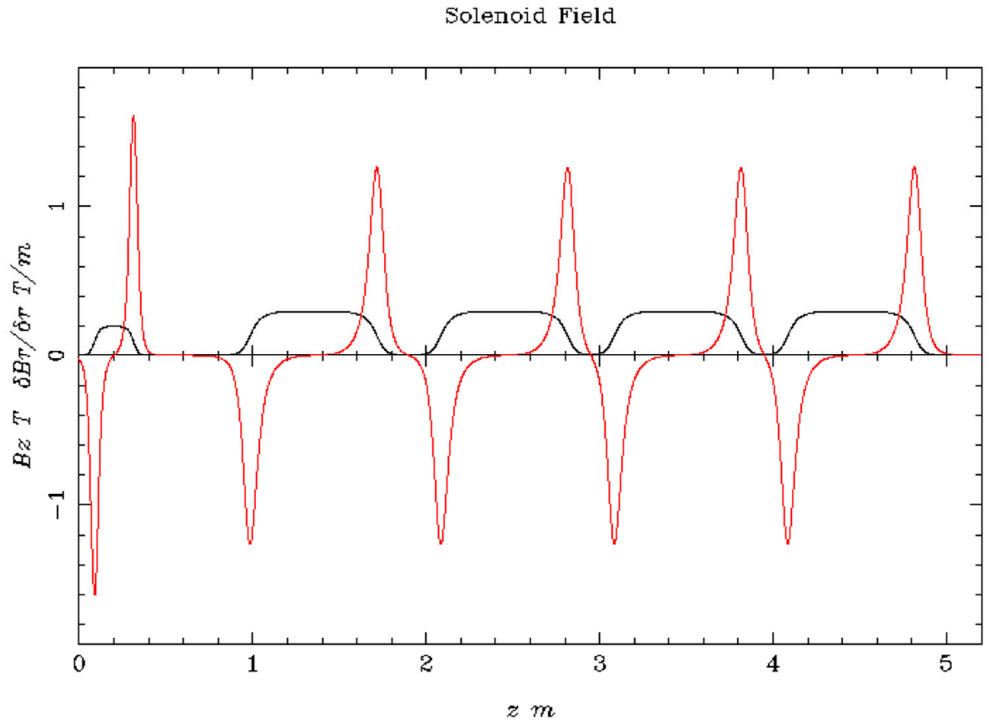

Figure 1. The solenoid field Bz (T), shown as the black line, and the magnetic field gradient dBr/dr (T/m), shown as the red line vs. the beam axis z (m) at the injector.

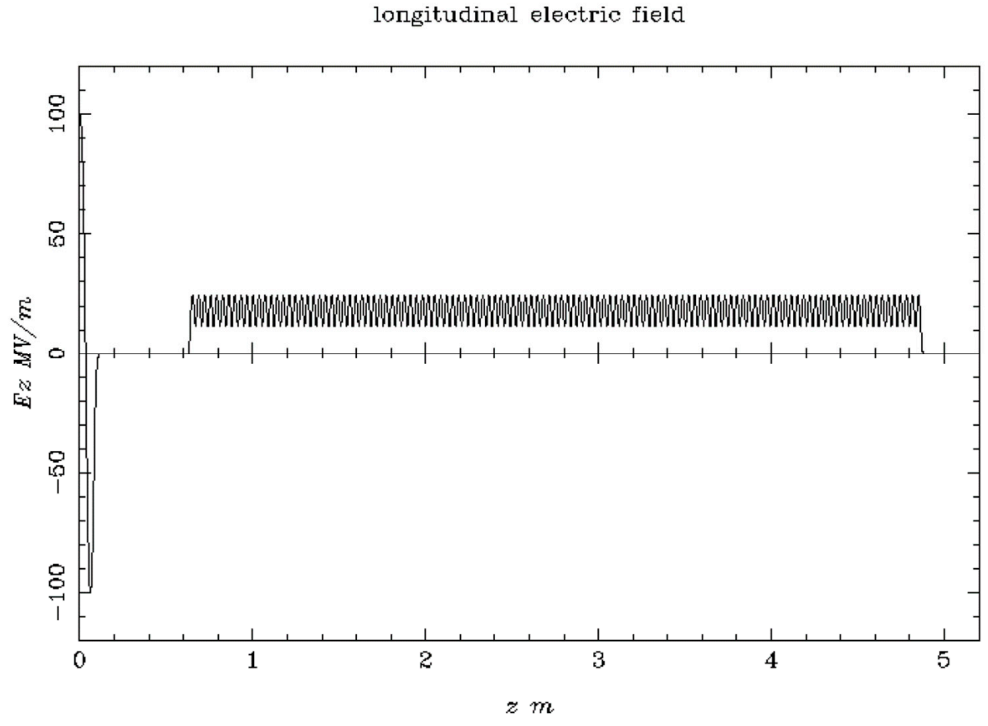

Figure 2. The longitudinal electric field Ez (MV/m) vs. the beam axis z (m).

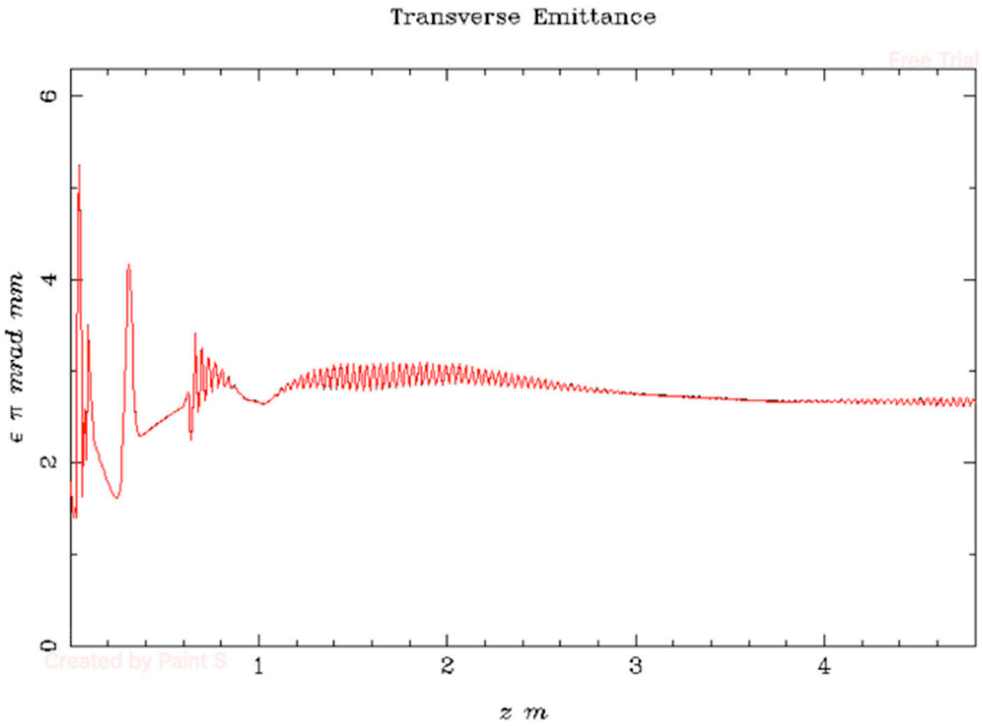

Figure 3. The electron beam transverse emittance vs. the beam axis z (m).

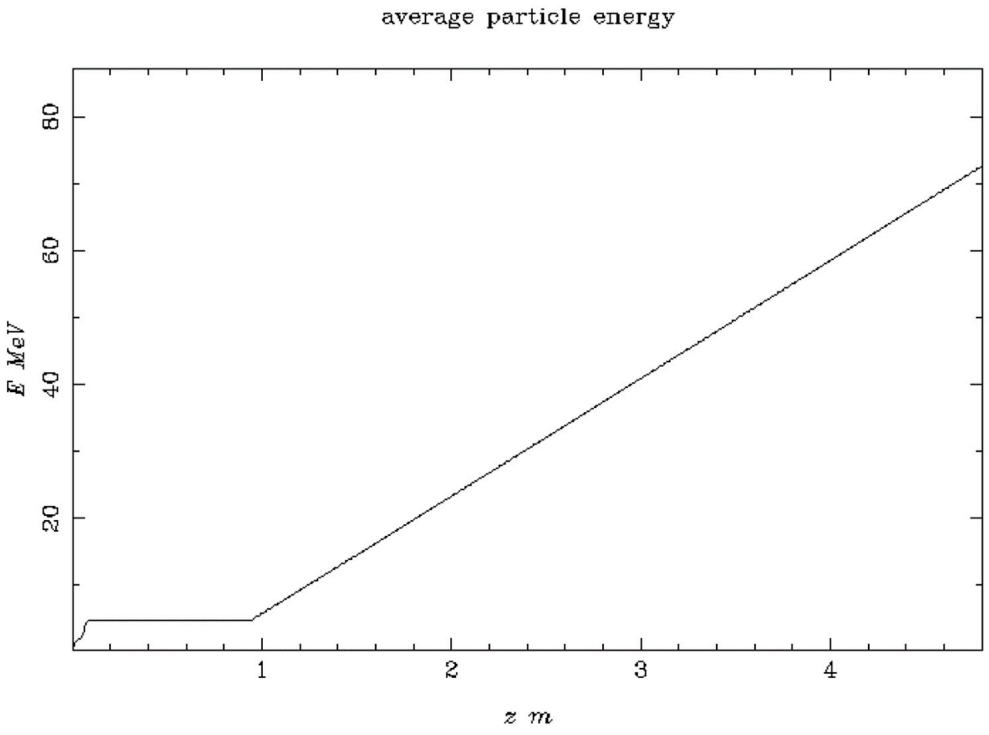

Figure 4. The average electron beam energy vs. the beam axis z (m).

2.3. Phantoms in Medical and Health Physics

The radiation dose measurement simulation and experimental tests in phantoms provide quality assurance for radiation therapy treatment [21,22]. The phantoms are formed by special materials and represent the equivalent human body in geometrical details and the approximate tissue composition.

In the context of radiation therapy quality assurance, a range of dosimeters, such as film, diodes and ionization chambers, along with tissue substitute phantoms, are utilized

to verify the accurate delivery of prescribed therapeutic doses. The water phantom has physical and radiological properties that are very similar to those of human soft tissue. Further, to study methods for treating moving tumors, organ motion phantoms are used to replicate periodic organ motion. This enables researchers to investigate and develop effective treatments for moving tumors [21]. The effective water atomic number closely approximates the effective atomic number of human tissues. Moreover, water phantoms proved to be valuable for acquiring beam profiles and measuring radiation doses, and they played a crucial role in the commissioning and quality assurance testing of linear accelerators and treatment planning systems [22].

In the realm of electron radiotherapy, selecting the right phantom material is crucial for precise dose measurements and effective treatment planning. PolyMethyl-MethAcrylate (PMMA), commonly known as acrylic or Plexiglas, emerges as a promising alternative to water in specific contexts, particularly low-energy electron beam dosimetry. The merits of PMMA as a water substitute and its preference over water are considered in certain radiation therapy scenarios. PMMA exhibits advantages that make it a compelling water substitute. Its density closely approximates that of water, rendering it suitable for crafting water-equivalent phantoms, a prerequisite for accurate dose measurements. Notably, PMMA demonstrates a comparable electron range to water for low-energy electron beams, particularly those under 10 MeV [23]. Additionally, PMMA showcases the potential to mitigate electron scattering effects due to its electron density's proximity to water's. This trait is especially advantageous for accurate dose measurements in low-energy electron beam dosimetry. Practically, PMMA offers accessibility, moldability for shaping into desired phantom geometries and cost-effectiveness. These practical attributes enhance its suitability as a phantom material, particularly where water is not the primary choice. Additionally, PMMA's moldability proves advantageous in designing phantoms with intricate geometries. For higher-energy electron and photon beams, water remains the reference medium due to its superior water-equivalence properties. In conclusion, PMMA presents a promising alternative to water in electron radiotherapy, especially in the low-energy spectrum.

2.4. Electron Dosimetry

Electron beam dosimetry stands at the forefront of modern radiation therapy, providing a pivotal role in delivering precise and targeted radiation doses to tumors and minimizing the impact on the healthy tissues around the beam spot. As a specialized field within medical physics, electron beam dosimetry focuses on the measurement and calculation of electron beam characteristics, enabling clinicians to design treatment plans tailored to each patient's unique anatomy and tumor location. With its ability to harness the distinctive properties of electron beams, electron dosimetry has revolutionized cancer treatment by enhancing treatment efficiency and optimizing patient outcomes.

2.4.1. Percentage Depth Dose (PDD) of Electron Beam

The electron beam central axis depth–dose curve provides a surface dose much higher than the high-voltage photon beams. The increasing electron beam depth of dose arrives at its maximum (z_{max}) at a certain known depth. The dose decreases rapidly after z_{max} and levels off at a lower dose tail due to the bremsstrahlung effect. These characteristics provide clinical advantages over conventional X-ray modalities in treating superficial tumors.

High-energy linear accelerators (linacs) typically generate electron beams in the energy range of 4–100 MeV. The electron beams delivered by the linear accelerator are almost monoenergetic, even though interactions with intermediate structures upon arrival at the patient, such as the accelerator tube exit window, shielding foils, monitor chambers, collimators and air, broaden the electron energy spectrum of the beams. These interactions lead to photon production (bremsstrahlung), contributing to the bremsstrahlung tail in the electron beam percentage depth dose (PDD) distribution. Upon initial contact with the patient, the electron beam for treatment has an incident mean energy lower than the electron

energy provided by the accelerator. The percentage depth dose (PDD) represents the ratio of the dose at a specific point on the central axis of an electron beam to the maximum dose on the central axis, multiplied by 100. This PDD value is usually measured for the nominal treatment distance, defined as the distance between the accelerator tube exit window and the patient's skin, and it depends on the electron beam characteristics, the field size and the energy, as shown in Figure 5 [24].

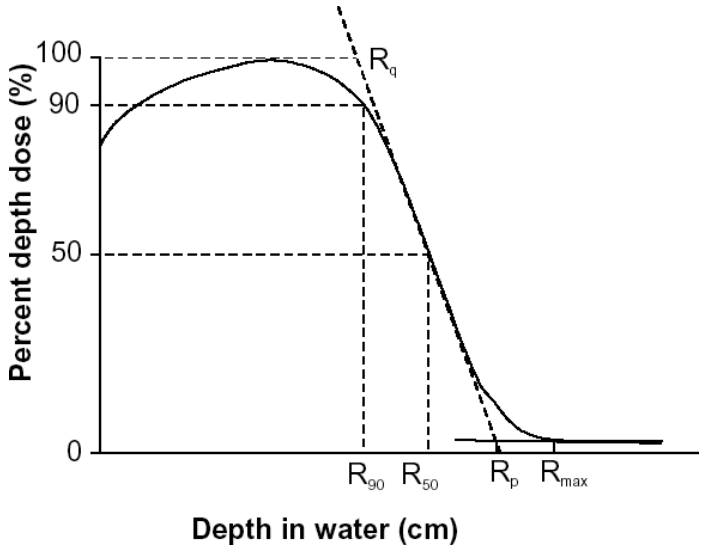

Figure 5. Typical electron beam percentage depth dose (PDD) curve illustrating the definitions of R_q, R_p, R_{max}, R_{50} and R_{90}.

The maximum range R_{max} is the largest penetration depth of electrons in the absorbing medium of irradiation. The R_{max} is defined as the depth where the extrapolation of the tail of the central-axis depth–dose curve meets the bremsstrahlung background.

The depths R_{90} and R_{50} are defined as depths on the electron percentage depth dose curve, corresponding to 90% and 50% values of the z_{max}, respectively.

2.4.2. Transverse Dose Profile

In electron radiotherapy, the transverse dose profile refers to the distribution of radiation dose delivered by an electron beam in the plane perpendicular to the beam's central axis. It represents how the dose is distributed across the patient's body or treatment field at a specific depth along the beam's path.

The transverse dose profile is a crucial parameter in treatment planning, as it directly affects the coverage of the target area (tumor) and the sparing of nearby healthy tissues. Clinicians use this information to ensure that the prescribed dose is accurately delivered to the tumor while minimizing radiation exposure to critical structures. The shape of the transverse dose profile depends on various factors, including the initial energy of the electron beam, the beam collimation, the beam scattering and the presence of any beam modifiers. For a well-defined and uniform dose distribution, the transverse dose profile should ideally have a flat and symmetrical shape, ensuring that the target area receives the intended dose.

Treatment planning systems and dosimetry measurements help characterize the transverse dose profile, providing valuable information for optimizing treatment plans and ensuring safe and effective electron radiotherapy. Additionally, advancements in technology and accurate beam modeling contribute to further refining the transverse dose profiles, leading to improved patient outcomes in electron radiotherapy treatments.

2.5. Electron Beam to Phantom Simulation Studies

For this study, the codes FLUKA and FLAIR based on Monte-Carlo (MC) simulation have been extensively used [25].

The FLUKA code is a general-purpose simulation code for the interaction and transport of hadrons, leptons and photons from keV to cosmic ray energies in any material [26]. No tuning on integral data, like calorimeter resolutions, thick target yields, etc., is performed. The obtained predictions have minimal free parameters, fixed for all energies and target/projectile combinations. Transport in a magnetic field is also performed. The FLUKA has a wide range of applications, spanning accelerator design and shielding, radiation protection, particle physics, dosimetry, detector simulation and hadron therapy.

The FLAIR code [27] is an advanced user-friendly interface for FLUKA to facilitate the editing of FLUKA input files, execution of the code and visualization of the output files.

2.6. Simulations for FLASH-RT

The beam characteristics and its delivered device geometry to the phantom/patient have followed the work of L. Guliano et al. [13]. Figure 6 presents the 3D design applicator for the electron beam delivery to the phantom cube used for the simulations in this work.

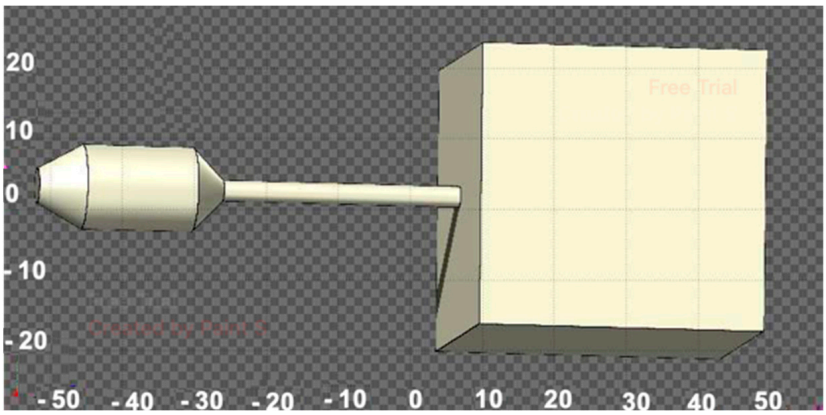

Figure 6. The 3D design applicator for the beam delivery to the phantom cube.

In that case, the electron beam exits from the linac and goes through a 55 μm thick titanium window that seals the linac vacuum. The source-to-surface distance (SSD) is defined as 60 cm, and a 40 × 40 × 40 cm^3 PMMA phantom is placed at the exit of the applicator. The delivered electron beam has a Gaussian distributed electron profile of (full-width at half-maximum) FWHM 3.4 mm on the x and y planes and a negligible mean angular spread. An energy cut-off for the transport and production of both electrons and photons was set to 10 keV (kinetic energy). Particles with an energy level below the threshold are not transported further. The expected dose per electron was evaluated in the PMMA phantom.

3. Dosimetry Results and Discussion

3.1. PMMA Applicator with PMMA Phantom

The first simulated results have been obtained with the applicator and phantom made from PMMA material. The 2D dose distribution plots, using a range of electron energies, including 5, 7 and 9 MeV, as well as higher energies of 50, 100 MeV and 1.2 GeV, are presented in Figures 7 and 8. It should be taken into consideration that in the 2D plot for the 1.2 GeV beam energy, the phantom dimension has been increased at the beam (*z* axis) to 140 cm.

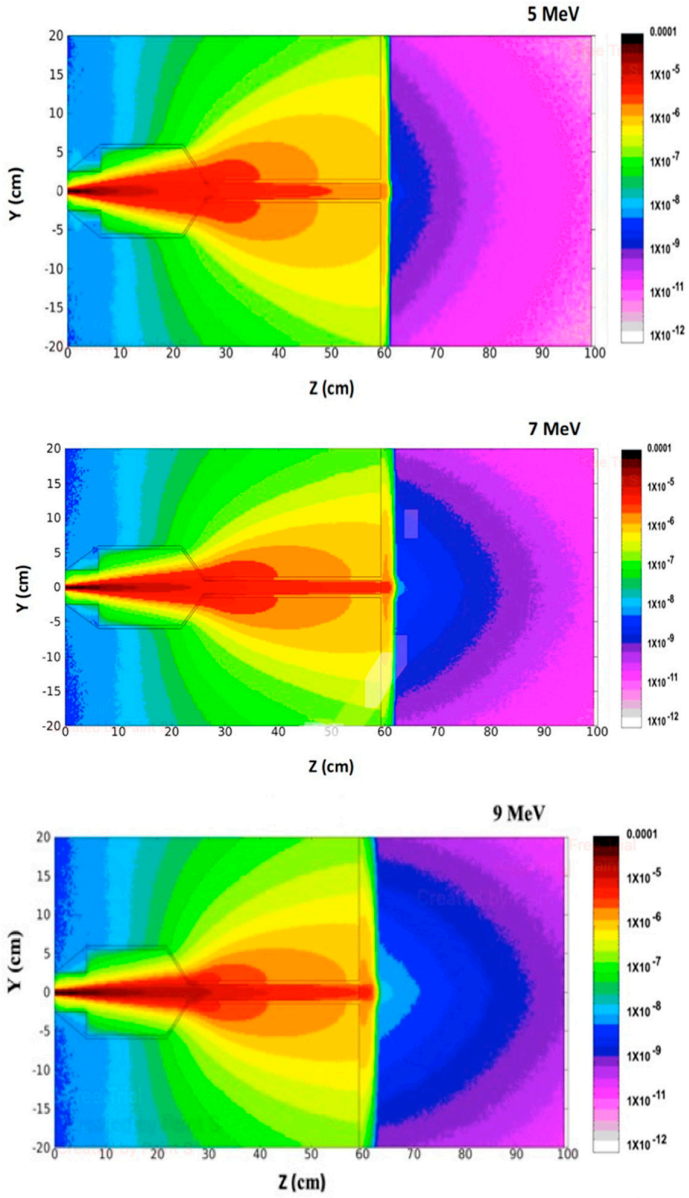

Figure 7. The 2D dose distribution plots using a range of electron energies, including 5, 7 and 9 MeV.

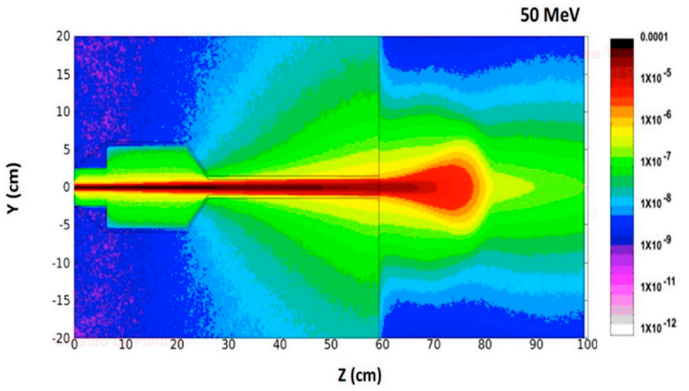

Figure 8. *Cont.*

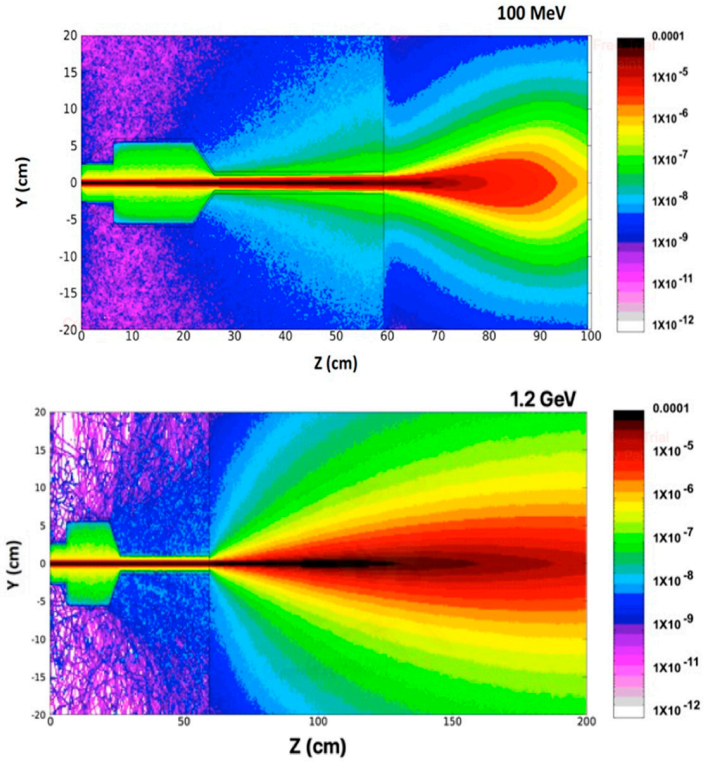

Figure 8. The 2D dose distribution plots using a range of electron energies, including 50, 100 MeV and 1.2 GeV. It is underlined that the phantom dimension has been increased at the *z* axis to 140 cm in the case of the 1.2 GeV beam energy.

3.2. Dose–Depth Distribution

It can be deduced, considering the dose distribution plots in Figures 7 and 8, that as the electron beam energy increases, the beam penetration depth increases, too. Notably, the 50, 100 MeV and mainly 1.2 GeV electron beams exhibit significantly greater depth as well as minimal beam loss outside the applicator.

The importance of exploring very-high-energy electron beams, that is, 50 MeV, 100 MeV and 1.2 GeV, lies in our quest to assess their potential suitability for treating deep-seated tumors.

As the electron beam energy increases from 50 to 100 MeV and then to 1.2 GeV, the beam appears much more focused, and an increased part of the beam energy is distributed to the phantom.

3.3. The Percentage Depth Dose (PDD) Curves (Gy vs. cm)

Simulation results for the 5, 7 and 9 MeV electron beams are presented in the following Figure 9, which reports the data of the dose, in Gy vs. cm, measured along the beam axis as a function of the depth within the phantom of PMMA material.

It is underlined that the PDD curves in Figure 9 represent the central part of the depth–dose distribution, which, in fact, includes the largest fraction of the dose inside the phantom.

Additionally, the FLASH effect parameters for the 5, 7, 9, 50, 100 MeV and 1.2 GeV electron beam energies have been obtained. In Table 3, the dose per pulse, the maximum instantaneous dose rate assuming a pulse duration of 4 μs, and the pulse repetition frequency of 250 Hz are presented. The last column of Table 3 presents the calculated average dose rate for the above-mentioned electron beam energies. The results of these energies define the FLASH regime.

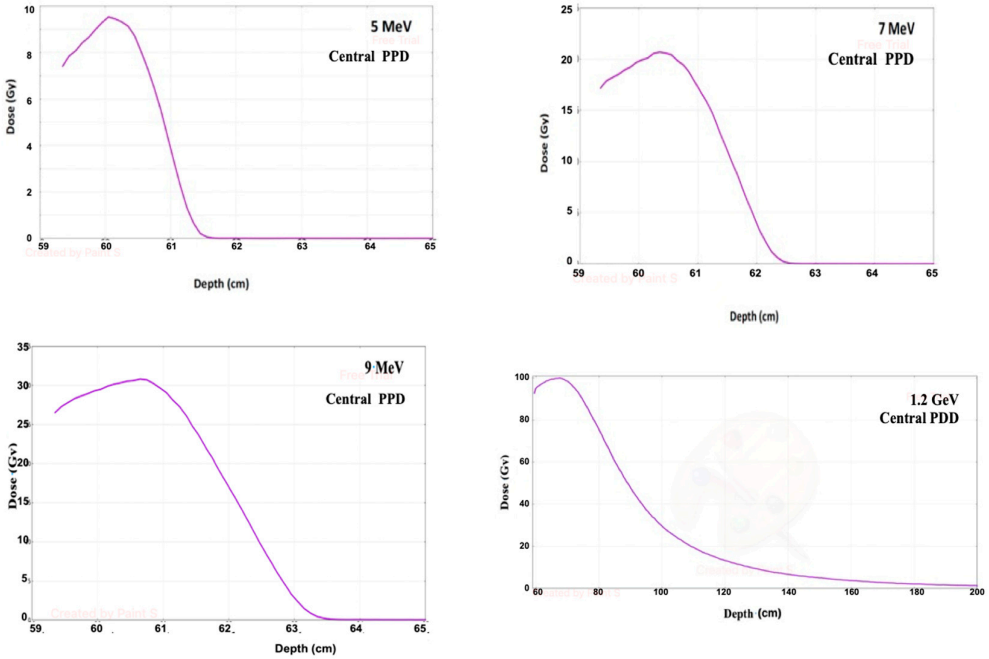

Figure 9. The dose–depth distribution plots for the electron energies, including 5, 7, 9 MeV and 1.2 GeV. It is underlined that, in the case of the 1.2 GeV beam energy plot, the phantom dimension has been increased at the *z* axis to 140 cm.

Table 3. The dose per pulse (Gy) and instantaneous dose rate (Gy/s), assuming a pulse duration of 4 μs and a pulse repetition frequency of 250 Hz, for the obtained average dose rate (Gy/s) at the electron beam energies of 5, 7, 9, 50, 100 MeV and 1.2 GeV. The FLASH effect regime area is highlighted.

Energy (MeV)	Maximum Peak Beam Current (mA)	Dose per Pulse (Gy)	Instantaneous Dose Rate (Gy/s) $\times$ 10^6	Average Dose Rate (Gy/s) $\times 10^3$
5	108	9.5	2.38	2.38
7	120	20.7	5.18	5.18
9	120	30.8	7.70	7.70
50	120	48.0	12.00	12.00
100	120	67.0	16.75	16.75
1200	120	99.0	24.75	24.75
			FLASH effect conditions	

The shapes of the depth–dose curves in Figure 9 are similar, defined by useful range parameters. R(opt) is the optimum thickness where the exit dose is equal to the entrance dose. At low beam energies penetrating low-Z materials, the X-ray background is negligible, and R(p) is essentially the same as R(ex), which is the extension of the tangent line to the depth axis. In the very-high-beam energy at 1.2 GeV, the dose–depth curve differs significantly from the low-energy one, penetrating to a depth of 200 cm inside the phantom.

The following Figure 10 presents the percentage depth dose (PDD) curve measured along the central axis of the beam for the 5, 7, 9, 50 and 100 MeV electron beams. The data were normalized to their maximum dose value.

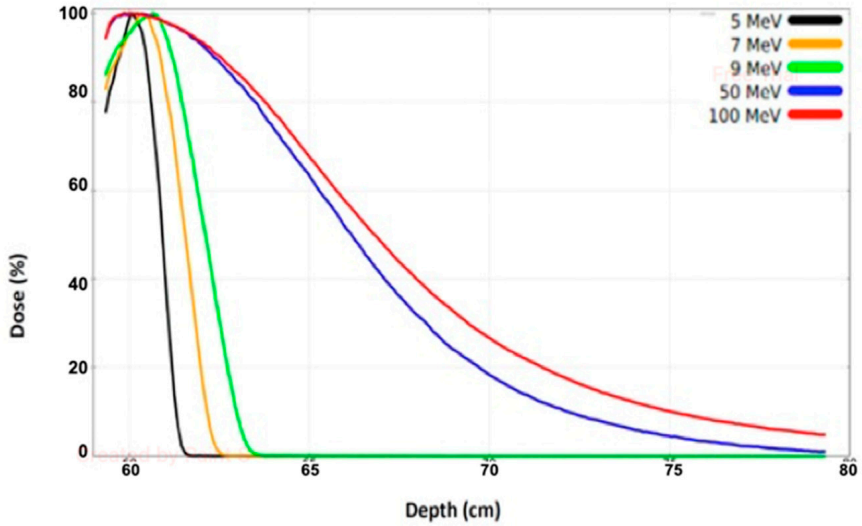

Figure 10. The percentage depth dose (PDD) plots for the electron beam energies of 5, 7, 9, 50 and 100 MeV, normalized to their maximum dose value.

3.4. Dose Profile vs. Phantom Depth

In order to determine the way the beam is distributed within the phantom, the beam profile plots along the beam central axis for the energies of 5, 7 and 9 MeV, as shown in Figure 11a–c. The depths R_{100}, R_{80} and R_{50} are defined as percentage depth doses on the electron percentage depth dose curve, corresponding to values of 100%, 80% and 50%, respectively.

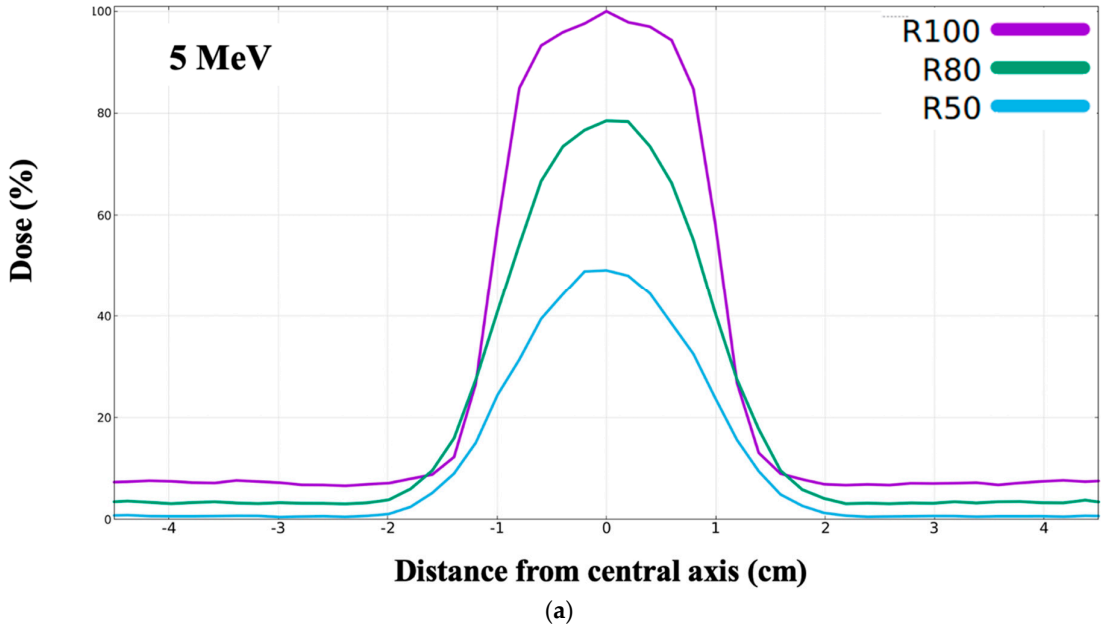

(**a**)

Figure 11. *Cont.*

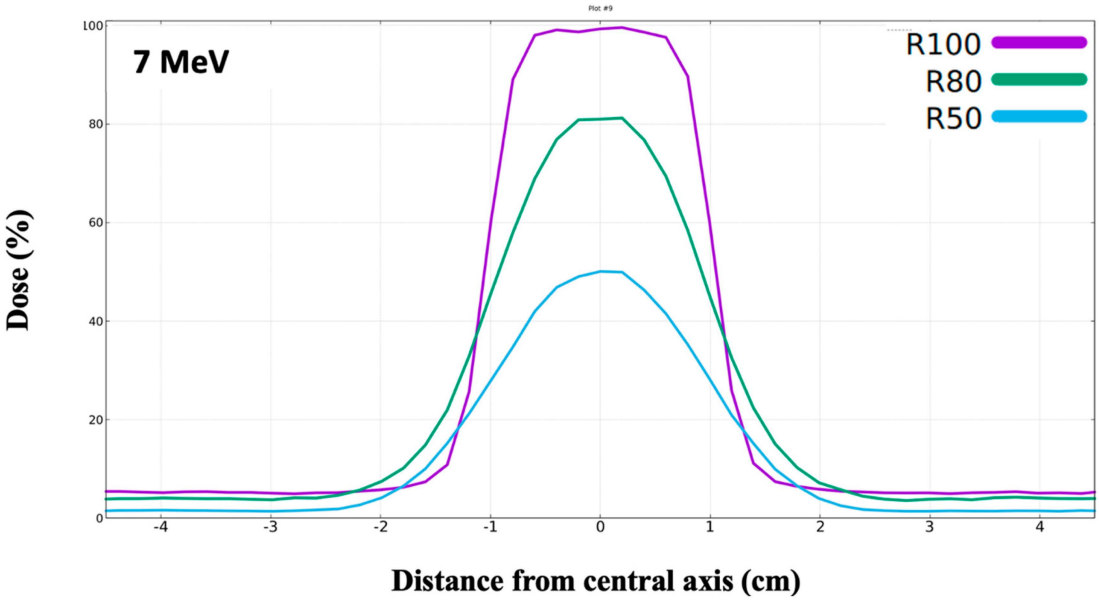

(**b**)

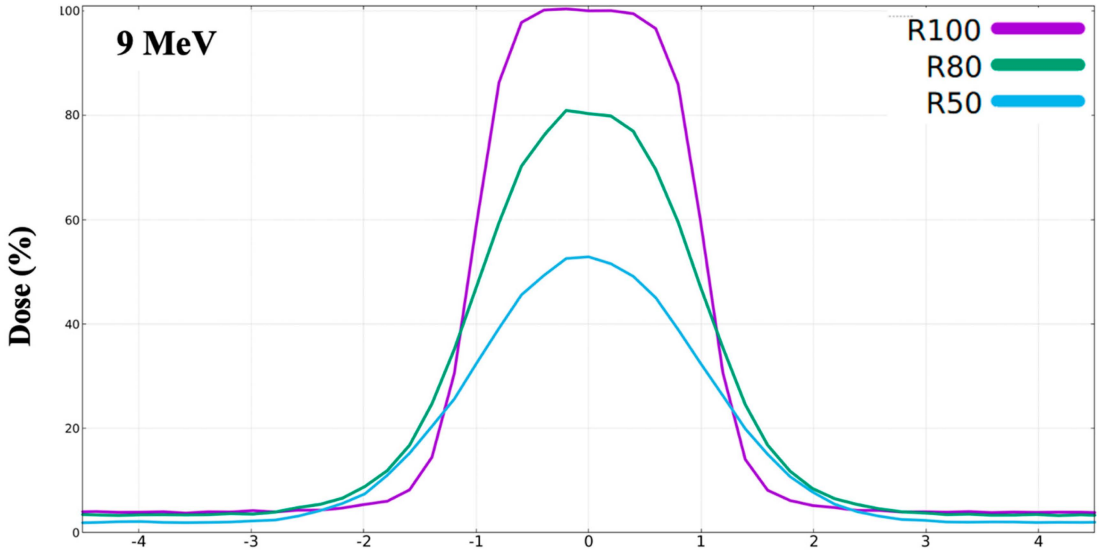

(**c**)

Figure 11. (**a**–**c**): The dose profile vs. the phantom depth for the respective electron beam energies of 5, 7 and 9 MeV.

Figure 11 shows that the beam profile is being progressively flattened and narrower as the electron beam energy increases from 5 to 9 MeV. This result is more emphatic for the case of depth R_{100}. The profile depths of R_{50} and R_{80} are following a slightly similar narrower shape with the beam energy change from 5 to 9 MeV.

4. Conclusions

In this study, the electron beam FLASH-RT injector design parameters were calculated with optimal operation simulations with the ASTRA code. An improvement should be considered for our future work to increase the beam charge as much as the accelerator beam stability permits without increasing the beam emittance. Further, the electron FLASH effect was investigated using the FLUKA simulation package across a range of electron beam energies. The impact of different beam applicators, each with varying material

compositions and geometries, with the primary aim of identifying the optimal electron beam characteristics for cancer treatment was examined.

Dose and beam characteristics were calculated for different electron energies of 5, 7, 9, 50, 100 MeV and 1.2 GeV in the PMMA phantom by studying the percentage depth dose (PDD) and dose profile plots with a well-defined applicator geometry.

It was determined that, for specific cancer treatments, the selection of materials with higher atomic numbers for the electron applicator could provide a more collimated beam. It is noteworthy that all the obtained results met the requirements of the FLASH conditions, with an average dose rate $\bar{D}$ >100 Gy/s, an in-peak dose rate of $\dot{D}p$ > 106, a pulse repetition frequency PRF > 100 Hz and an irradiation time t_i < 100 ms.

It is recommended that future experimental studies be conducted to validate the simulation outcomes of this research. These additional investigations will contribute to a better and more comprehensive perception of the electron FLASH effect mechanism on biological tissues and its potential applications in cancer treatment.

Author Contributions: Conceptualization, methodology, writing—original draft preparation, supervision, funding acquisition, and project administration, E.G. and N.G.; software, E.T. and A.B.; validation, D.B. and N.V.; formal analysis and data curation, M.M.; writing—review editing and visualization, N.G. All authors have read and agreed to the published version of the manuscript.

Funding: This research received no external funding.

Data Availability Statement: The data will be made available upon request from the corresponding author after 1 July 2025.

Conflicts of Interest: The authors declare no conflict of interest.

References

1. Gianfaldoni, S.; Gianfaldoni, R.; Wollina, U.; Lotti, J.; Tchernev, G.; Lotti, T. An Overview on Radiotherapy: From Its History to Its Current Applications in Dermatology. *Open Access Mac. J. Med. Sci.* **2017**, *5*, 521. [CrossRef] [PubMed]
2. Tsujii, H. Overview of Carbon-ion Radiotherapy. *IOP Conf. Ser. J. Phys. Conf. Ser.* **2017**, *777*, 012032. [CrossRef]
3. Tian, X.; Liu, K.; Hou, Y.; Cheng, J.; Zhang, J. The evolution of proton beam therapy: Current and future status (Review). *Mol. Clin. Oncol.* **2017**, *8*, 15–21. [CrossRef]
4. Gagnebin, S.; Twerenbold, D.; Pedroni, E.; Meer, D.; Zenklusen, S.; Bula, C. Experimental determination of the absorbed dose to water in a scanned proton beam using a water calorimeter and an ionization chamber. *Nucl. Instrum. Methods Phys. Res. Sect. B Beam Interact. Mater. At.* **2010**, *268*, 524–528. [CrossRef]
5. Bourhis, J.; Sozzi, W.J.; Jorge, P.G.; Gaide, O.; Bailat, C.; Duclos, F.; Patin, D.; Ozsahin, M.; Bochud, F.; Germond, J.F.; et al. Clinical translation of FLASH radio- therapy: Why and how? *Radiother. Oncol.* **2019**, *139*, 11–17. [CrossRef]
6. Pratx, G.; Kapp, D.S. A computational model of radiolytic oxygen depletion during FLASH irradiation and its effect on the oxygen enhancement ratio. *Phys. Med. Biol.* **2019**, *64*, 185005. [CrossRef] [PubMed]
7. Favaudon, V.; Caplier, L.; Monceau, V.; Pouzoulet, F.; Sayarath, M.; Fouillade, C.; Poupon, M.F.; Brito, I.; Hupe, P.; Bourhis, J.; et al. Ultrahigh dose-rate FLASH irradiation increases the differential response between normal and tumor tissue in mice. *Sci. Transl. Med.* **2020**, *12*, 1671. [CrossRef] [PubMed]
8. Varnava, M.; Jun-ichi Saitoh Tashiro, M.; Kubo, N.; Okano, N.; Kawamura, H.; Ohno, T. Dose–volume constraints for head-and-neck cancer in carbon ion radiotherapy: A literature review. *Cancer Med.* **2023**, *12*, 8267–8277. [CrossRef] [PubMed]
9. Mohamad, O.; Sishc, B.J.; Saha, J.; Pompos, A.; Rahimi, A.; Story, M.D.; Davis, A.J.; Kim, D.W.N. Carbon Ion Radiotherapy: A Review of Clinical Experiences and Preclinical Research, with an Emphasis on DNA Damage/Repair. *Cancers* **2017**, *9*, 66. [CrossRef] [PubMed]
10. Debowski, M.; Murphy, A.; Jones, J. Electron Therapy. Reference Article. Radiopaedia.org. Available online: https://radiopaedia.org/articles/67623 (accessed on 23 June 2023).
11. Kokurewicz, K.; Brunetti, E.; Welsh, G.H.; Wiggins, S.M.; Boyd, M.; Sorensen, A.; Chalmers, A.J.; Schettino, G.; Subiel, A.; DesRosiers, C.; et al. Focused very high-energy electron beams as a novel radiotherapy modality for producing high-dose volumetric elements. *Sci. Rep.* **2019**, *9*, 10837. [CrossRef] [PubMed]
12. Kaiser, A.; Eley, J.G.; Onyeuku, N.E.; Rice, S.R.; Wright, C.C.; McGovern, N.E.; Sank, M.; Zhu, M.; Vujaskovic, Z.; Simone, C.B.; et al. Proton Therapy Delivery and Its Clinical Application in Select Solid Tumor Malignancies. *J. Vis. Exp.* **2019**, *144*, e58372. [CrossRef] [PubMed]
13. Giuliano, L.; Franciosini, G.; Palumbo, L.; Aggar, L.; Dutreix, M.; Faillace, L.; Favaudon, V.; Felici, G.; Galante, F.; Mostacci, A.; et al. Characterization of Ultra-High-Dose Rate Electron Beams with ElectronFlash Linac. *Appl. Sci.* **2023**, *13*, 631. [CrossRef]

14. Montay-Gruel, P.; Petersson, K.; Jaccard, M.; Boivin, G.; Germond, J.-F.; Petit, B.; Doenlen, R.; Favaudon, V.; Bochud, F.; Bailat, C.; et al. Irradiation in a flash: Unique sparing of memory in mice after whole brain irradiation with dose rates above 100 Gy/s. *Radiother. Oncol.* **2017**, *124*, 365–369. [CrossRef] [PubMed]
15. Floettmann, K. *ASTRA, A Space Charge Tracking Algorithm, Version 3.2*; DESY: Hamburg, Germany, 2017.
16. Gazis, N.; Tanke, E.; Trachanas, E.; Apostolopoulos, T.; Karagiannaki, A.; Pramatari, K.; Telali, I.; Tzanetou, K.; Gazis, E. Photocathode study of the CompactLight Collaboration for a novel XFEL development. In *International Journal of Modern Physics: Conference Series 2020 50—International Conference on Applications of Nuclear Techniques ("CRETE19") Crete, Greece, 5–15 June 2019*; World Scientific Publishing Company: Singapore, 2020. [CrossRef]
17. Chevallay, E.; Csatari, M.; Dabrowski, A.; Doebert, S.; Egger, D.; Fedosseev, V.; Mete, O.; Olvegaar, M.; Petrarca, M. PHIN photo-injector as the CLIC drive beam source. In *Journal of Physics, Conference Series, 2nd International Conference on Particle Physics in Memoriam Engin Arık and Her Colleagues, Istanbul, Turkey, 20–25 June 2011*; Doğuş University: Istanbul, Turkey, 2012; Volume 347.
18. Mete, O. Study and Experimental Characterization of a Novel Photo Injector for the CLIC Drive Beam. Ph.D. Thesis, École Polytechnique Fédérale de Lausanne, Lausanne, Switzerland, 2011.
19. Alves, M.; Arnault, C.; Auguste, D.; Babigeon, J.L.; Blot, F.; Brossard, J.; Bruni, C.; Cavalier, S.; Cayla, J.N.; Chaumat, V.; et al. PHIL photoinjector test line. *J. Instrum.* **2012**, *8*, T01001. [CrossRef]
20. Li, J.; Asova, G.; Isaev, I.V.; Groß, M.; Hakobyan, L.; Ivanisenko, Y.; Khojoyan, M.; Klemz, G.; Kourkafas, G.; Krasilnikov, M.; et al. Emission Studies of Photocathode RF Gun at PITZ. In Proceedings of the ICAP2012, Rostock-Warnemünde, Germany, 19–24 August 2012.
21. Halloran, A. Dosimetric Advantages of Personalized Phantoms for Quality Assurance and Research in Radiation Dose Measurements. Master's Thesis, Louisiana State University: Baton Rouge, LA, USA, 2015. Available online: https://repository.lsu.edu/gradschool_theses/1227/ (accessed on 23 June 2023).
22. Yadav, N.; Singh, M.; Mishra, S.P. Tissue-equivalent materials used to develop phantoms in radiation dosimetry: A review. *Mater. Today Proc.* **2021**, *47*, 7170–7173. [CrossRef]
23. International Atomic Energy Agency. Absorbed Dose Determination in External Beam Radiotherapy An International Code of Practice for Dosimetry Based on Standards of Absorbed Dose to Water. Vienna. 2000. Available online: https://www-pub.iaea.org/MTCD/Publications/PDF/TRS398_scr.pdf (accessed on 23 June 2023).
24. Strydom, W.; Parker, W.; Olivares, M. Chapter 8 Electron Beams: Physical and Clinical Aspects. Available online: http://www-naweb.iaea.org/nahu/DMRP/documents/Chapter8.pdf (accessed on 23 June 2023).
25. Raychaudhuri, S. Introduction to Monte Carlo Simulation. Available online: https://www.informs-sim.org/wsc08papers/012.pdf (accessed on 23 June 2023).
26. fluka.cern. About FLUKA | The Official CERN FLUKA Website. Available online: https://fluka.cern/about (accessed on 23 June 2023).
27. fluka.cern. The Flair Graphical User Interface | The Official CERN FLUKA Website. Available online: https://fluka.cern/documentation/running/flair-gui (accessed on 25 August 2023).